machines

*Article*

# Effect of Slot Jet Flow on Non-Axisymmetric Endwall Cooling Performance of High-Load Turbines

**Kun Du [1,2,3,4], Yihao Jia [1], Hui Song [1], Lei Chen [5], Qian Zhang [5], Tingting Cui [5] and Cunliang Liu [1,3,4,*]**

1 School Power and Energy, Northwestern Polytechnical University, Xi'an 710072, China
2 Yangtze River Delta Research Institute of NPU, Northwestern Polytechnical University, Taicang 215400, China
3 Shaanxi Key Laboratory of Thermal Sciences in Aero-Engine System, Northwestern Polytechnical University, Xi'an 710129, China
4 NPU-KAI International Joint Laboratory of Advanced Aero-Engine Thermal Structure, Northwestern Polytechnical University, Xi'an 710129, China
5 AECC Sichuan Gas Turbine Establishment, Chengdu 610500, China
* Correspondence: liucunliang@nwpu.edu.cn

**Abstract:** As vane inlet temperatures and turbine loadings are increasing, the aerodynamic and thermal management for the endwalls of gas turbines have received increased attention. Non-axisymmetric endwalls are becoming popular due to their proficient capabilities to modify the secondary flow fields and to change the film cooling performance on the endwalls. In this study, by considering the interaction between mainstream and purge flow based on non-axisymmetric endwall contouring, the numerical research model used in the present research was established. Based on the validated numerical method, the influence of the non-axisymmetric endwall contouring on the film-cooling effectiveness and aerodynamic characteristics was studied. Furthermore, the effect of different inclination angles on the film-cooling performance of the contoured endwalls was also investigated. The results indicate that for the high-load turbine vane used in this research, various types of non-axisymmetric endwall contouring can alter the aero-dynamic characteristics and cooling performance simultaneously. By inhibiting the secondary flows, non-axisymmetric endwall contouring can reduce the total cascade pressure loss coefficient by 0.305%. In addition, non-axisymmetric endwall contouring can significantly enhance the effective coverage area of purge flow up to 28.29%, and the endwall near the suction side can achieve better cooling performance. Finally, non-axisymmetric endwall contouring can improve the protective effect of large-angle purge flow.

**Keywords:** non-axisymmetric; film cooling; aerodynamic characteristics; purge flow; numerical simulation



**Citation:** Du, K.; Jia, Y.; Song, H.; Chen, L.; Zhang, Q.; Cui, T.; Liu, C. Effect of Slot Jet Flow on Non-Axisymmetric Endwall Cooling Performance of High-Load Turbines. *Machines* **2023**, *11*, 134. https://doi.org/10.3390/machines11020134

Academic Editor: Antonio J. Marques Cardoso

Received: 6 December 2022
Revised: 31 December 2022
Accepted: 16 January 2023
Published: 18 January 2023



## 1. Introduction

In recent years, to increase the thermal effectiveness of gas turbines due to the current vast energy needs, the turbine inlet temperature and pressure have become incredibly high [1–3]. Additionally, the technology used in diffusion burners has been updated to minimize $NO_x$ emissions, and it can cause a steadier turbine inlet temperature distribution and increase the heat load of endwall surfaces in turbines [4]. Hence, the efficient and stable operation of gas turbines requires an in-depth investigation of the cooling and aerodynamic characteristics at turbine endwalls.

The application of high-load turbines can obtain a substantial thrust-to-weight ratio but can also enhance the lateral pressure gradient in cascade passage, which aggravates the typical three-dimensional flow features within a turbine passage—the secondary flows of endwalls. Denton [5] pointed out that 2/3 of endwall losses come from the boundary-layer fluids of the cascades, and secondary flow loss can account for more than 50% of aerodynamic losses in the first-stage stator blades of turbines with a small aspect ratio. To reduce secondary flow loss, some noted scholars have devoted themselves to unraveling the fundamentals of non-axisymmetric endwalls. Rose [6] first proposed the basic principle of endwall contouring design in 1994: the regional profile of the endwall near the pressure side forms humps to accelerate the fluid and forms valleys near the suction side to decelerate the fluid to reduce the uneven distribution of static pressure in the endwall, and to inhibit the development of the secondary flows. Subsequently, R.R. Company and Durham University took planar cascade as the research object and proposed the "FAITH Endwall Forming Method" [7]. In addition to investigating the characteristics of the flow fields of endwalls, many scholars have combined the optimization algorithm with endwall contouring to distribute several control points on the surfaces of endwalls. By altering the parameters of the control points and setting some optimization goals for iteration, an endwall profile that meets anticipated requirements is ultimately obtained. After analyzing the influence of local endwall contouring on aerodynamic performance using the global sensitivity method, Chen et al. [8] stated that under the action of flow acceleration, the passage vortex is far away from the endwall, and the aerodynamic loss core is suppressed.

Due to the separate processing and installation of multiple gas turbine components, there are inherent gaps between the combustion chamber and the first-stage guide vane, as well as between the guide vane and the rotor blade. In engineering applications, to prevent gas from invading the clearance area and to protect the downstream endwall at the same time, the coolant needs to be extracted from the compressor [9,10] and shot into the mainstream flow through a slot. Zhao et al. [11] experimentally studied the effect of purge flow and main flow interaction. The results pointed out that the purge flow promotes the generation of the passage vortex near the suction side. Sundaram et al. [12] performed experiments to determine that at a constant coolant-to-mainstream mass flow ratio (MFR), the purge-cooling effectiveness and coolant spreading area were both enhanced when the width of the slot decreased. Du et al. [13] documented that the tangential ejection angle significantly influenced the effectiveness of endwall cooling. Tao et al. [14] reported that with the help of a contracted cross-sectional geometry, the purge slot could accelerate the coolant to improve the cooling effectiveness dramatically. Babu et al. [15] used numerical methods to reveal the development mechanism of the pressure-side boundary layer under the influence of non-axisymmetric contouring endwall with purge flow and found that endwall contouring can provide very effective endwall protection. Zhang et al. [16] combined the Kriging model with the NSGA-II algorithm and studied the influence of swirl purge flow on non-axisymmetric endwall. The results show that two optimal contours are able to increase the adiabatic effectiveness of the endwall separately by 3.518% and 2.177%, respectively, but the flat endwall achieved the best phantom cooling performance. Tao et al. [17] numerically studied the gas–thermal properties of non-axisymmetric endwalls with purge flow and found that there were significant differences in the gas–thermal properties of different endwall regions after contouring. Mensch et al. [18] discovered that endwall contouring inhibited the development of the passage vortex, weakened the mixing of the slot jet and the mainstream, and, thus, improved the effectiveness of film cooling.

Up until now, there have been few studies considering the impact of non-axisymmetrical endwall contouring on cooling performance in endwalls with purge flow. Furthermore, the effect of the slot ejection angle on cooling performance within a non-axisymmetrical endwall is seldom considered. As established above, based on the endwall contouring technology of the differential pressure method, the aerodynamic and cooling characteristics of endwall contouring and the effect of the jet ejection angle on the cooling performance of the contoured endwall are numerically studied in this paper.

## 2. Computational Method and Validation

### *2.1. Geometrical Model*

In this research, the computational model was obtained by magnifying the first-stage guide vane of a typical commercial engine by a factor of nine [12]. Figure 1 plots the geometric model used in the experiment and numerical simulation. A baseline flat endwall is used as a benchmark for the non-axisymmetric endwalls. D is the diameter of the film hole in reference [12]. To reveal the effects of the purge flow more clearly, the computational model in this paper does not arrange the leading edge's film holes. The geometric parameters of the model are consistent with those in the literature. The specific geometric parameters and boundary conditions of the cascade are listed in Table 1.

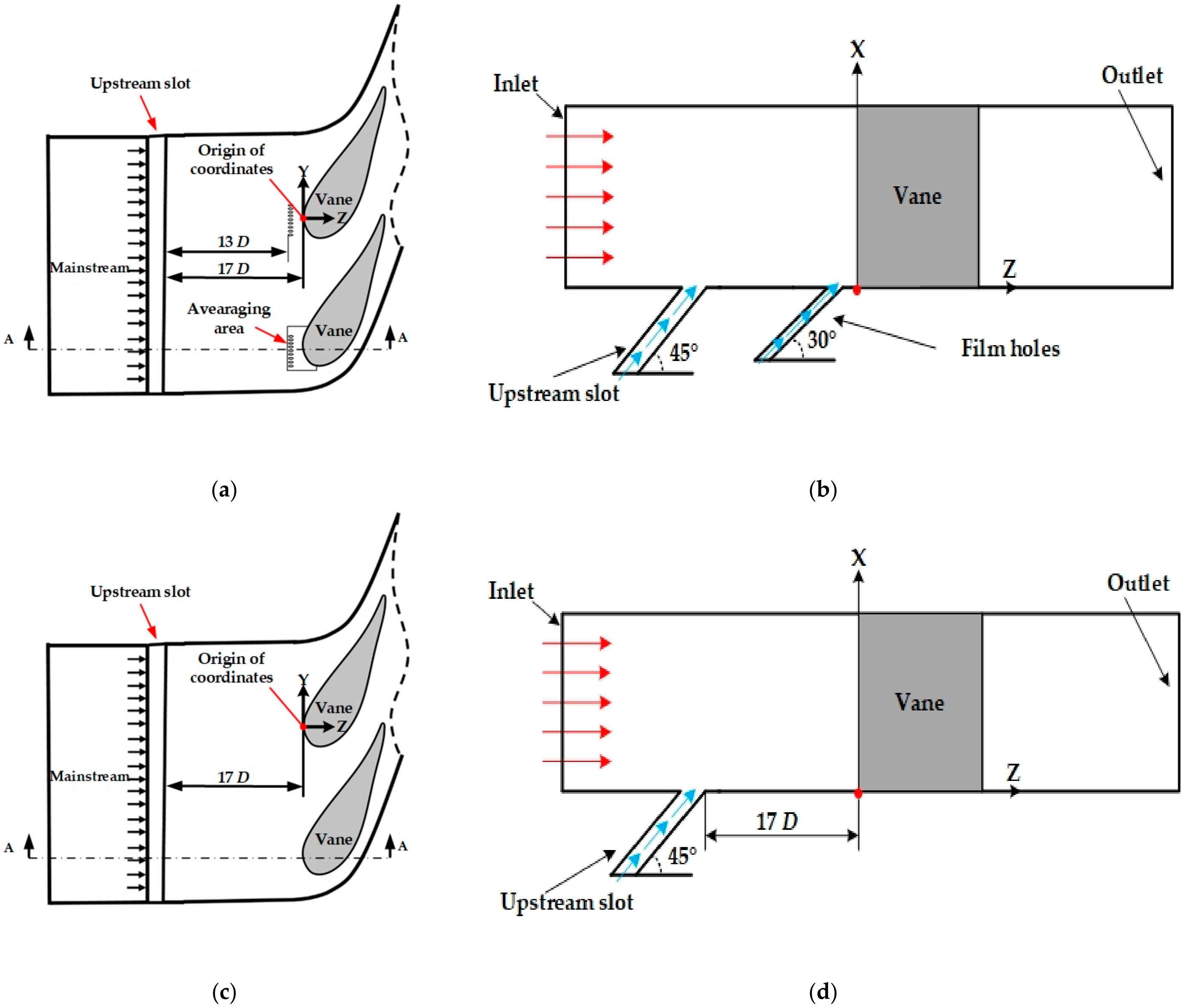


**Figure 1.** Schematic diagram of the vane with an upstream slot. (**a**) Experimental model. (**b**) A-A cross-section of the experimental model. (**c**) Computational model. (**d**) A-A cross-section of the computational model.

**Table 1.** Geometric parameters.

| Parameters | Value |
|---|---|
| Chord length of blade C | 594 mm |
| Axial chord of blade $C_{ax}$ | 293 mm |
| Pitch, P/C | 0.77 |
| Span/Chord, S/C | 0.93 |
| Upstream slot width | 0.024 C |
| Hole, L/D | 8.3 |
| Inlet and exit angles | 0° & 72° |
| Hole diameter D | 4.6 mm |

*2.2. Turbulence Model Validation and Boundary Conditions*

Grid refinement is employed for all of the solid walls to better resolve the flow details. The O-type mesh is generated to discretize the solid walls of the computation domains to ensure that the y+ value is in an appropriate range. To provide fully developed inlet conditions, such as the boundary layer, velocity, and turbulence, the length of the inlet section is determined to be 0.75 times that of the chord length. To prevent backflow, the length of the outlet section was 1.2 times that of the chord length. All of the solid wall surfaces are adiabatic without slipping. Table 2 provides the specific boundary conditions of the cascade from the experiment.

**Table 2.** Computational boundary conditions.

| Parameters | Value |
|---|---|
| Mainstream inlet total temperature | 333.19 K |
| Mainstream inlet total pressure | 107.64 kPa |
| Coolant inlet total temperature | 293.15 K |
| $Re_{in}$ | $2.1 \times 10^5$ |
| Inlet Ma | 0.017 |
| Inlet turbulence intensity | 1% |
| Outlet Ma | 0.085 |
| Outlet static pressure | 107 kPa |
| Flow ratio(coolant/mainstream) | 0.6% |

The specific definitions of the formulas used in this study are listed below:

$$\eta = (T_\infty - T_{aw})/(T_\infty - T_c) \tag{1}$$

$$M = (\rho_c V_c)/(\rho_\infty V_\infty) \tag{2}$$

$$MFR = m_c/m_\infty \tag{3}$$

$$C_p = \frac{P - P_1}{\frac{m_\infty}{m_\infty + m_c} P^*_{0,\infty} + \frac{m_c}{m_\infty + m_c} P^*_{0,c} - P_1} \tag{4}$$

$$\xi = \frac{\frac{m_\infty}{m_\infty + m_c} P^*_{0,\infty} + \frac{m_c}{m_\infty + m_c} P^*_{0,c} - P^*_1}{P^*_1 - P_1} \tag{5}$$

where $T_{aw}$, $T_\infty$, and $T_c$ are the wall adiabatic temperature, mainstream temperature, and coolant temperature, respectively; $\rho_c$ and $\rho_\infty$ are the densities of the coolant and mainstream fluid; $V_c$ and $V_\infty$ are the velocities of the coolant and the main flow, respectively; $m_c$ and $m_\infty$ are the mass flows of the main flow and cooling flow, respectively; and $P^*_{0,\infty}$ is the total inlet pressure of the mainstream, $P^*_{0,c}$ is the total inlet pressure of the slot jet, $P$ is the local static pressure, $P_1$ is the outlet's static pressure, and $P^*_1$ is the outlet's total pressure, respectively.

Before the contouring, to verify the numerical method and assure the credibility of the predicted results, the three-dimensional Reynolds-Averaged Navier–Stokes (RANS) must select turbulence models based on flow characteristics. We have minutely com-pared the predictions of standard k-ω, SST k-ω, standard k-ε, and RNG k-ε to experiment in previous study [19]. The experimental result come from Sundaram et al. [12] at a blowing ratio of 1.0 of film holes and 0.3 of the upstream slot.

On the other hand, Figure 2 presents a quantitative comparison of area-averaged (the region is shown in Figure 1) effectiveness for the experimental model along the whole leading edge region at the slot's blowing ratio is 0.3. The standard k-ε model, standard k-ω model, and RNG k-ε model are found to overestimate the film cooling effectiveness at a higher blowing ratio. On the contrary, there is an underestimation of the diffusion of coolant at a lower blowing ratio. The SST k-ω model achieved the highest simulation accuracy, which is similar to the previous turbulence model verification result [19]. Thus, all of the numerical calculation in this paper adopt the SST k-ω turbulence model. In the experiment, the blowing ratio is used to manipulate the purge flow, but most studies on purge flow currently adopt the mass flow ratio. Therefore, with the exception of the blowing ratio used to verify the numerical method in this paper, the mass flow ratio is used in the subsequent numerical studies.

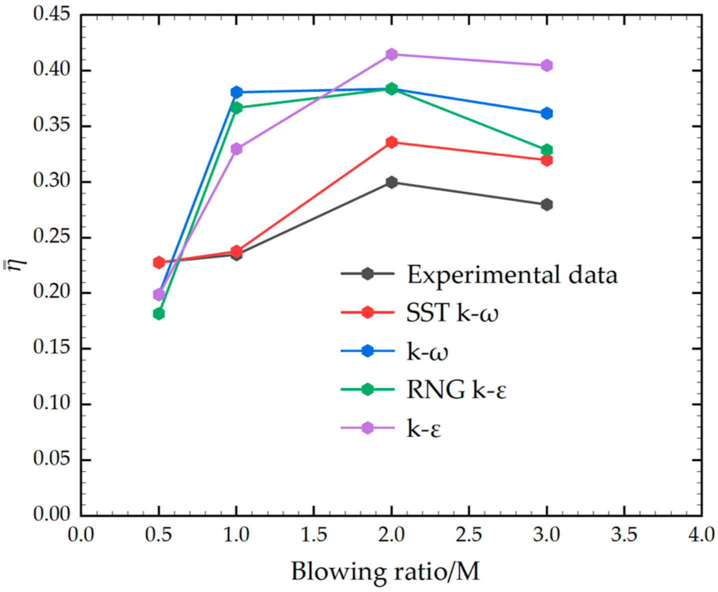


**Figure 2.** The area averaged cooling effectiveness of the leading edge region under different film hole-blowing ratios.

## *2.3. Mesh Independence Verification*

The numerical simulation results are significantly affected by the number of grids in the computational domain. To ensure reliable simulation results and to save computing resources, this section uses grid numbers of 3 million, 4 million, 5 million, and 6 million to carry out independent verification. During refinement, the grids increase in the same proportions along the X, Y, and Z directions. The average film-cooling effectiveness on the whole surface of the endwall is shown in Table 3:

**Table 3.** Average cooling effectiveness for different grid numbers.

| Grid Numbers | $\eta$ |
|---|---|
| $3 \times 10^6$ | 0.0652 |
| $4 \times 10^6$ | 0.0655 |
| $5 \times 10^6$ | 0.0658 |
| $6 \times 10^6$ | 0.0659 |

The verification results show that when the total grid number is 5 million, reliable calculation results can be obtained. Considering the simulation accuracy and the consumption of computing resources, this paper selects a grid number of 5 million for numerical simulation.

## *2.4. Non-Axisymmetric Endwall (NEC) Design*

Using the pressure difference method in combination with the static pressure distribution of the flat endwall, the non-axisymmetric endwall (NEC) is modeled using the trigonometric function. The basic steps are as follows:

(1) The static pressure distribution of the flat endwall for a non-purge flow is obtained numerically(as shown in Figure 3);

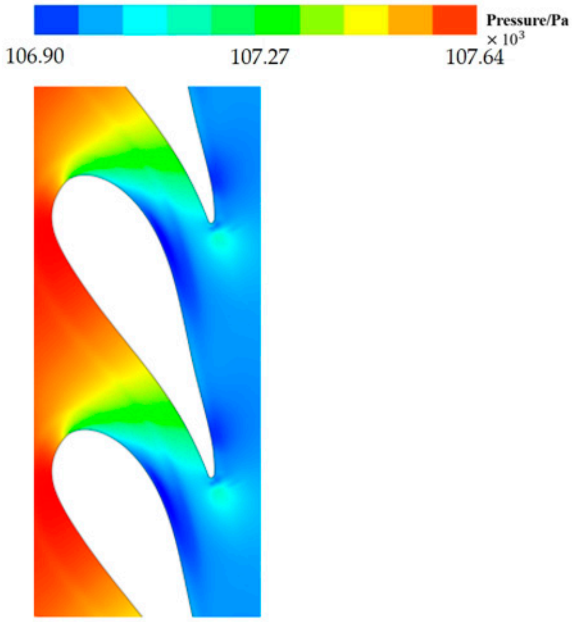


**Figure 3.** Static pressure distribution on the endwall.

(2) Axial control function;

$$\Delta p = \max(P_{ps} - P_{ss}) \tag{6}$$

$$A(z) = C * H * \frac{P_{ps} - P_{ss}}{\Delta p} \tag{7}$$

where $H$ represents the span of the vane, and $C$ controls the radial amplitude of the endwall profile, which is selected by the percentage of span. $P_{ps}$ and $P_{ss}$ are the static pressure at the blade root along the pressure side and suction side, respectively. At the same time, the b-spline curve is used to fit Equation (7) to ensure a smooth and continuous endwall surface.

As shown in Figure 4, 17 control lines are distributed from the inlet to the outlet of the vane passage. Figure 3 demonstrates that in the range of 30% to 70% $C_{ax}$, the circumferential pressure gradient is more prominent, so in this field (Figure 4, area 1), the contouring precision should be improved, and more control lines should be distributed. However, it can be seen that the radial amplitude of the first control line is 0, which is different from our expectations. The second line is maintained at a $C_{ax}$ distance of 0.5% from the leading edge to avoid the problem.

(3) Half-cycle circumferential function;

$$X_1(y,z) = A(z) sin\left[\frac{y - \frac{a(z)+b(z)}{2}}{a(z) - b(z)}\right] \tag{8}$$

(4) Full cycle circumferential control function:

$$X_2(y,z) = -A(z) sin\left[2\pi \frac{y - b(z)}{a(z) - b(z)}\right] \tag{9}$$

$$X_3(y,z) = A(z) sin\left[2\pi \frac{y - b(z)}{a(z) - b(z)}\right] \tag{10}$$

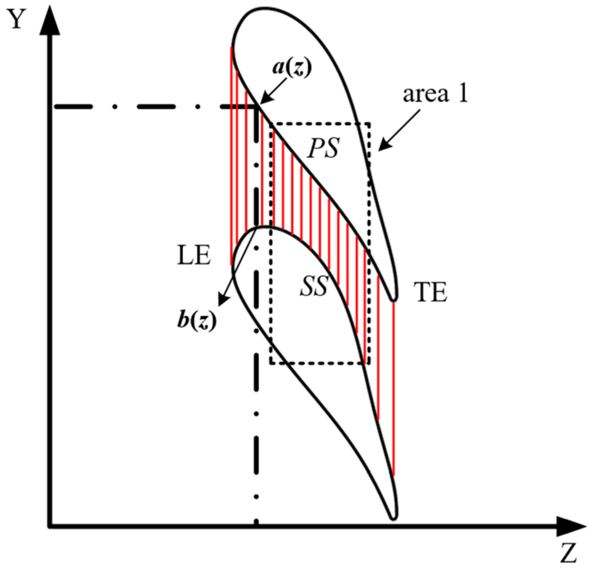


**Figure 4.** Distribution of asymmetric control lines on the end wall.

Figure 5 illustrates four cases of non-axisymmetric endwall contouring, where Case 1 is modeled by the half-cycle circumferential control function ($X_1(y,z)$), Case 2 is modeled by local contouring at 10%-to-100% $C_{ax}$ via the half-cycle circumferential control function ($X_1(y,z)$). Case 3 and 4 are the result of $X_2(y,z)$ and $X_3(y,z)$, respectively. Figure 6 shows the local grid diagram with a non-axisymmetrical endwall.

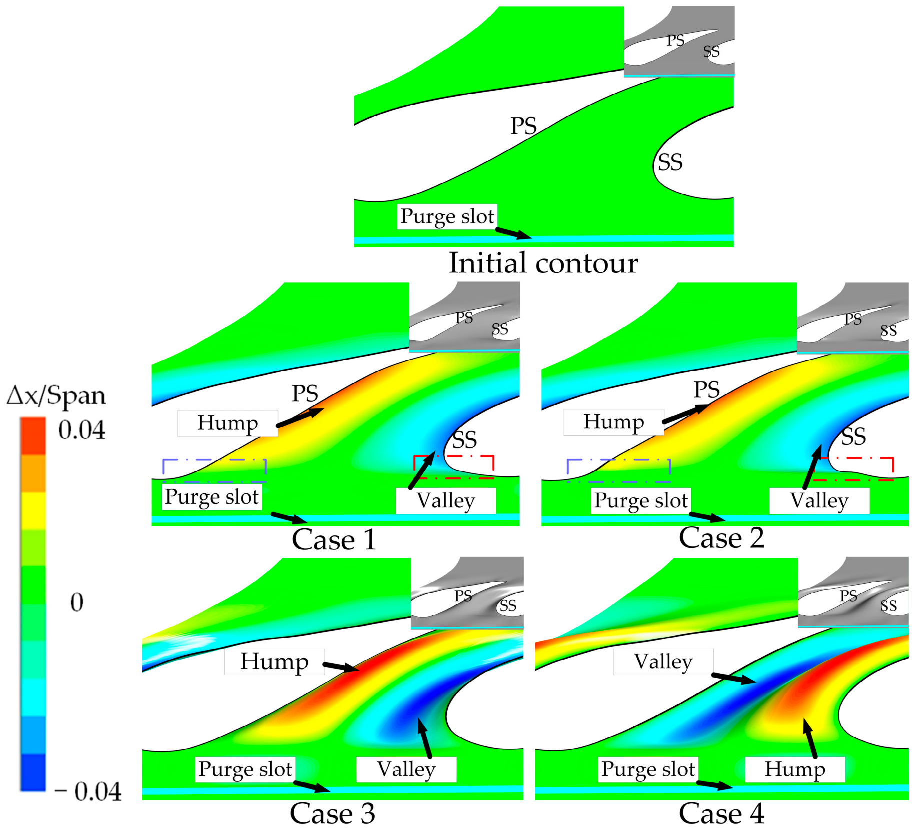


**Figure 5.** Contoured endwall height distribution.

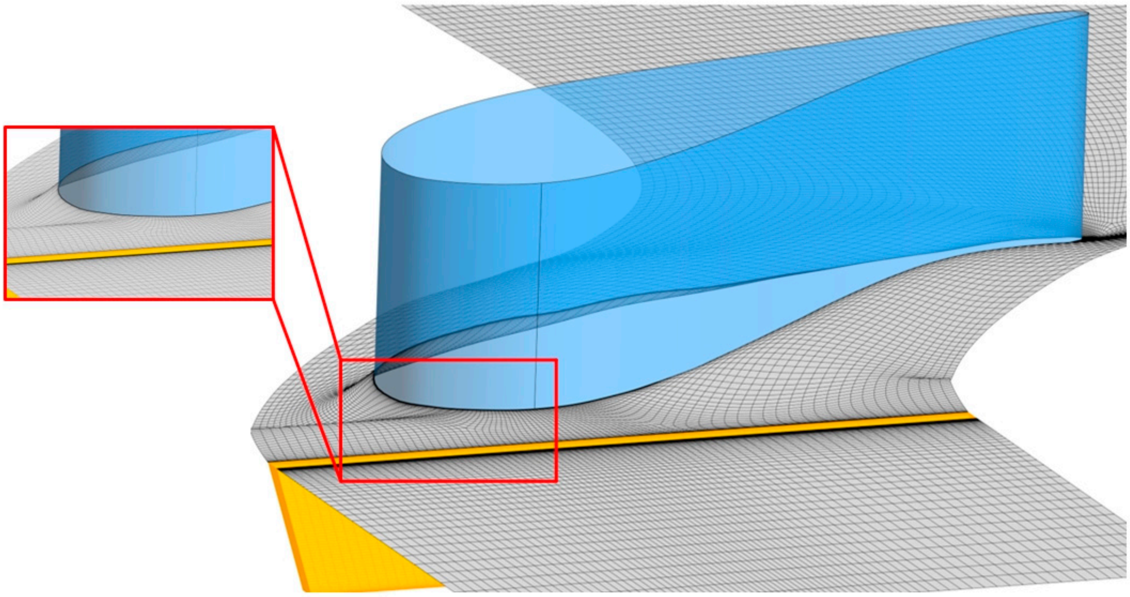

**Figure 6.** Computational mesh.

## 3. Results

### *3.1. Flow Field and Aerodynamic Analysis*

The aerodynamic performance and cooling characteristics of endwalls are affected by the secondary flow structures and the interactions between the purge flow and mainstream flow. Figure 7 clearly elucidates the static pressure coefficient at the root of the vane. The results point out that the NEC can significantly alter the static pressure at the root of the vane near the suction side but has almost no impact near the pressure side and that the half-cycle circumferential function can greatly reduce the circumferential pressure gradient.

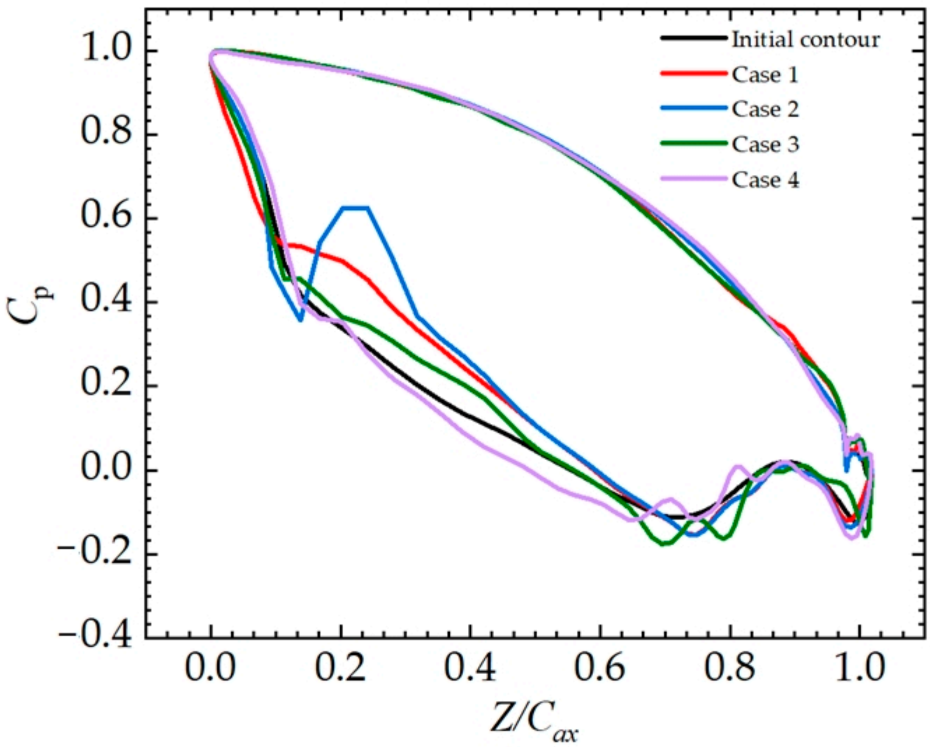


**Figure 7.** The coefficient distributions for static pressure.

When $0.1 < Z/C_{ax} < 0.7$, both Case 1 and Case 2 decelerate and boost the secondary flows due to the valley near the suction side, and the circumferential pressure difference decreases. During the range of $0 < Z/C_{ax} < 0.65$, for Case 3, because of the valley on the side of the suction side, the secondary flows slow down and increase the static pressure. As for Case 4, during the range of $0 < Z/C_{ax} < 0.1$, the lateral differential pressure is reduced, and at the position of $0.1 < Z/C_{ax} < 1.0$, the overall transverse pressure difference is increased on account of the hump.

On the other hand, it is vital to clarify the impact of different NECs on the passage vortex. Figure 8 depicts the axial vortex distribution of various NECs at the four position sections: the leading edge, 0.1 $C_{ax}$, 0.4 $C_{ax}$, and 0.7 $C_{ax}$.

$$\Omega = \omega_z C / U_{\text{Inlet}} \tag{11}$$

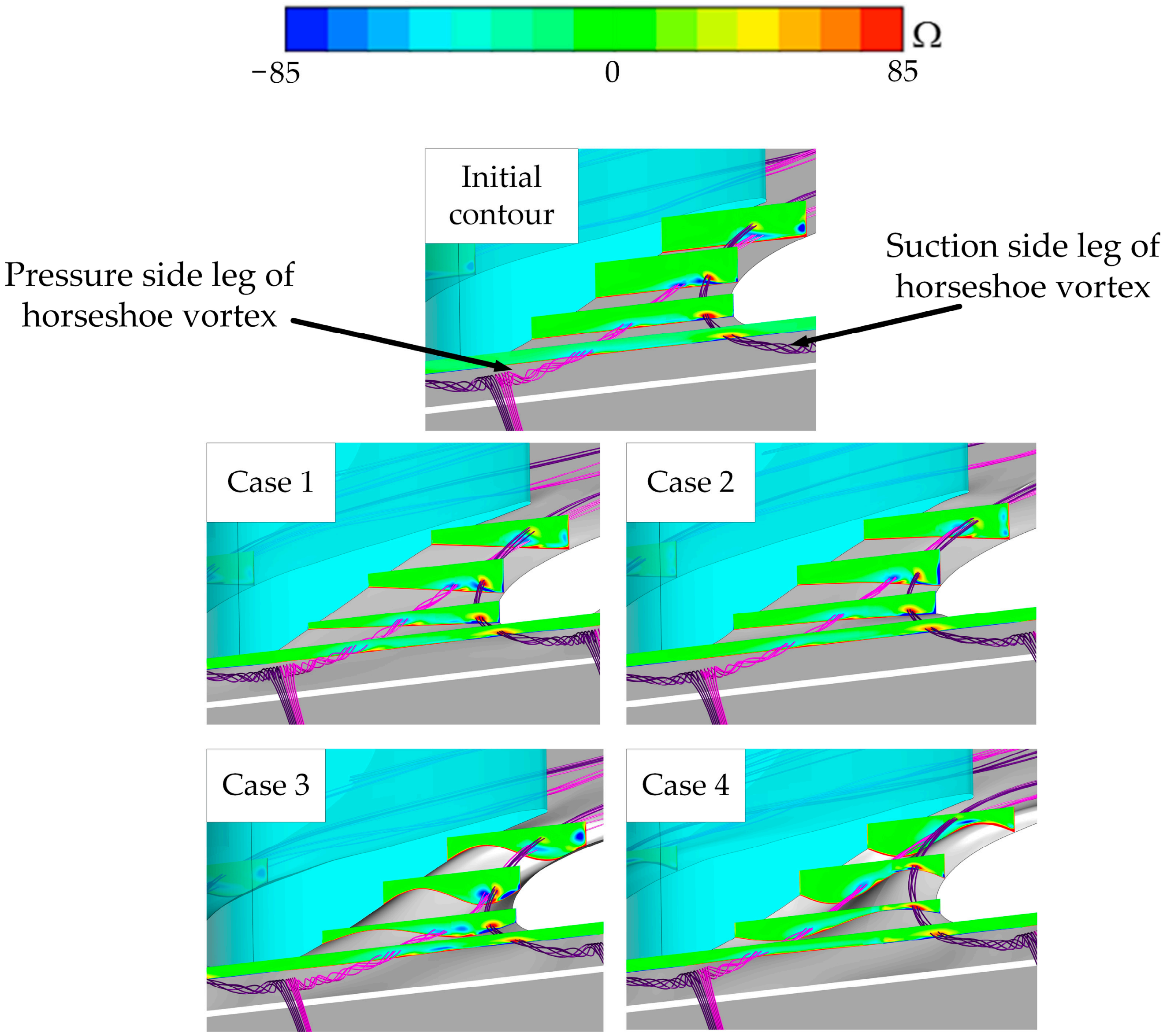


**Figure 8.** Vorticity distributions at LE, 0.1 $C_{ax}$, 0.4$C_{ax}$, and 0.7 $C_{ax}$ sections.

The consequences portray how the NECs could hinder the development of the horseshoe vortex. In the section of the leading edge, there is no noticeable difference in the horseshoe vortex. At the 0.4 $C_{ax}$ and 0.7 $C_{ax}$ cross-sections, Cases 1, 2, and 4 show the attenuation of the passage vortex loss core. Among them, Cases 1 and 2 inhibit the development of the passage vortex because of half-cycle contouring, which extremely reduces the circumferential pressure gradient, and Case 4 forms a hump between the suction-side and the pressure-side legs of the horseshoe vortex, destroying the evolution of the pressure-side leg of the horseshoe vortex, limiting it in the valley, and then weakening the strength of the passage vortex. Case 3 creates a hump between the pressure-side leg of the horseshoe vortex and the pressure side, forcing the pressure-side leg of the horseshoe vortex to approach the suction side. It is worth mentioning that compared to Case 1, Case 2 dilutes the suction-side leg of the horseshoe vortex.

Figure 9 plots the limit streamlines of the coolant and the mainstream flow under different NECs, clearly revealing the intermixing and transport of flows. The incoming flow is separated into two legs: the pressure-side leg and the suction-side leg of the horseshoe vortex. At the flat endwall, the suction-side leg of the horseshoe vortex flows to the suction side under the action of the transverse pressure gradient. The pressure-side leg of the horseshoe vortex continually absorbs the low-energy fluid in the region near endwall to institute the passage vortex. The blue arrow indicates the position where the pressure-side leg of the horseshoe vortex reaches the suction side. On the whole, Cases 1 and 2 significantly reduce the circumferential pressure gradient and inhibit the development of the pressure-side leg of the horseshoe vortex. In addition, due to the lack of a small value valley buffer, Case 2 creates a low-pressure region at 10% $C_{ax}$, where the secondary flows briefly converge (as shown in Figure 9c). As for Case 3, because of hump contouring between the pressure-side leg of the horseshoe vortex and the pressure side, the pressure-side leg of the horseshoe vortex reaches the suction side in advance. In Case 4, due to the formation of a hump between the suction-side leg and pressure-side leg of the horseshoe vortex, the pressure-side leg of the horseshoe vortex is confined in the valley to impede development. Meanwhile, a part of the pressure-side leg of the horseshoe vortex climbs along the hump and then converges with the suction-side leg of the horseshoe vortex to form a stagnation region (as shown in Figure 9e), which increases aerodynamic losses.

The total pressure loss coefficient tells the flow loss via the examination of the reduction of the total pressure in the cascade. Table 4 records the reduction percentage of the average total pressure loss coefficient at the outlet and is based on a flat endwall. It can be seen that Cases 1, 2, and 3 can lessen the total pressure loss by a maximum of 0.305%, indicating that the reduction of the circumferential pressure difference can inhibit the growth of secondary flows. Moreover, although Case 4 weakens the strength of the pressure-side leg of the horseshoe vortex, the increase in the circumferential pressure difference is not conducive to reducing aerodynamic losses.

**Table 4.** Non-dimensional total pressure loss coefficient.

| Case | $\Delta\xi$/% |
|---|---|
| Case 1 | 0.114 |
| Case 2 | 0.272 |
| Case 3 | 0.305 |
| Case 4 | −1.800 |

To sum up, for the high-load turbine vane selected in this paper, under the condition of purge flow cooling, an NEC based on the differential pressure method can reduce the aerodynamic losses of the cascade by lowering the transverse pressure difference, and Case 3 has the best aerodynamic characteristics. On the contrary, Case 4 achieves the worst aerodynamic performance.

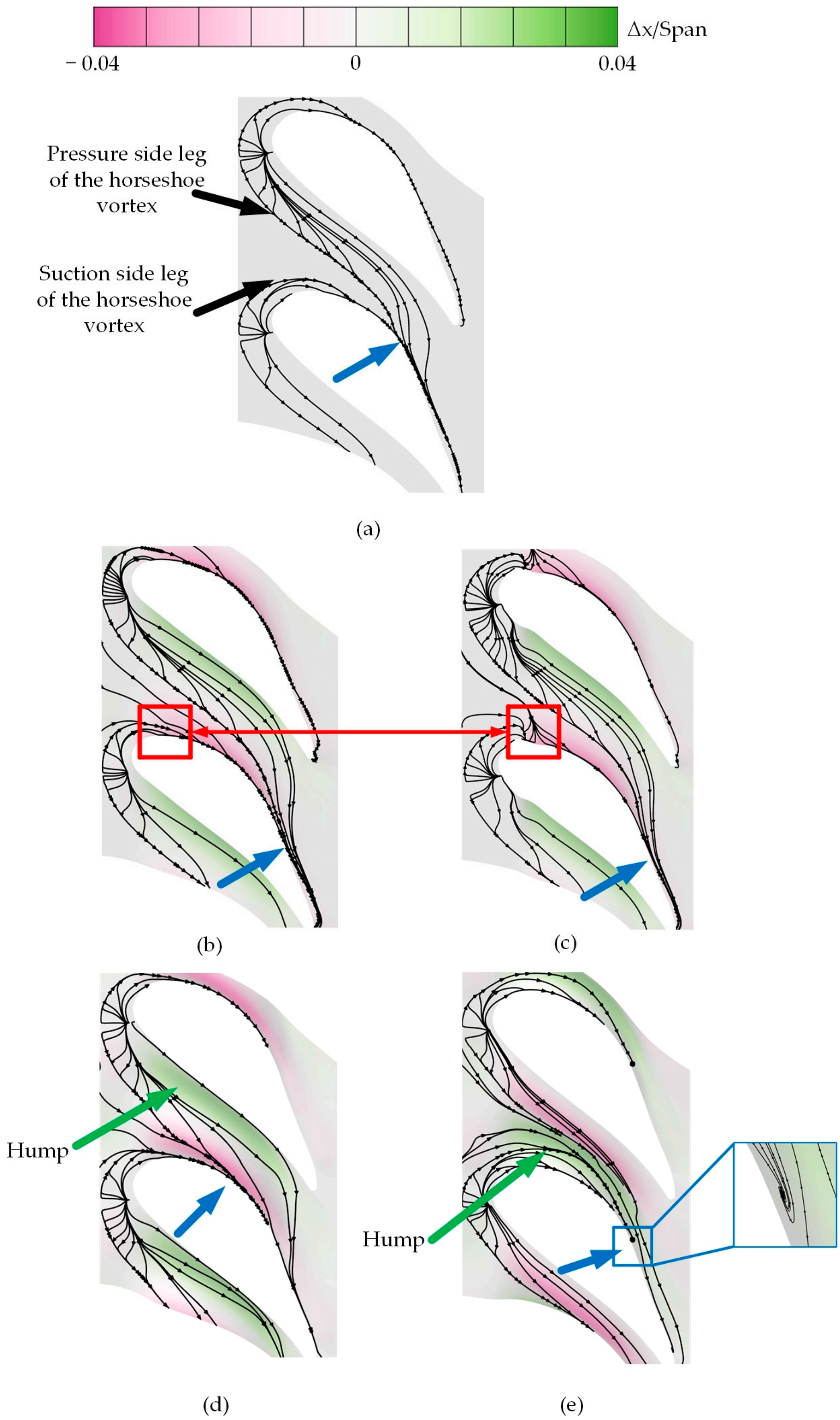


**Figure 9.** Limiting streamlines on the endwall. (**a**) Initial contour. (**b**) Case 1. (**c**) Case 2. (**d**) Case 3. (**e**) Case 4.

### *3.2. Film Cooling Performance Analysis*

Figure 10 points out that with the limit of the suction-side leg and pressure-side leg of the horseshoe vortex, the purge flow is not evenly distributed on the endwall and has an insufficient coverage effect on the leading edge of the vane and the endwall near the pressure side, constantly moving toward the suction side. Due to the constrained transverse pressure gradient in Case 1 and Case 2, the enrolling ability of the passage vortex to purge flow is inhibited, and the coolant is restricted to the area closer to the endwall near the suction side. In Case 3, owing to the hump around the pressure side, the pressure-side leg of the horseshoe vortex is closer to the suction surface, the purge flow is also sucked by it, and the cooling effect decreases immensely. In Case 4, due to the hump near the suction side, the purge flow is slightly affected by the pressure-side leg of the horseshoe vortex and achieves great coverage. It should be noted that in a location in Case 4, where the hump contouring amplitude is the largest, the film cooling effectiveness is lower than it is in the surrounding area.

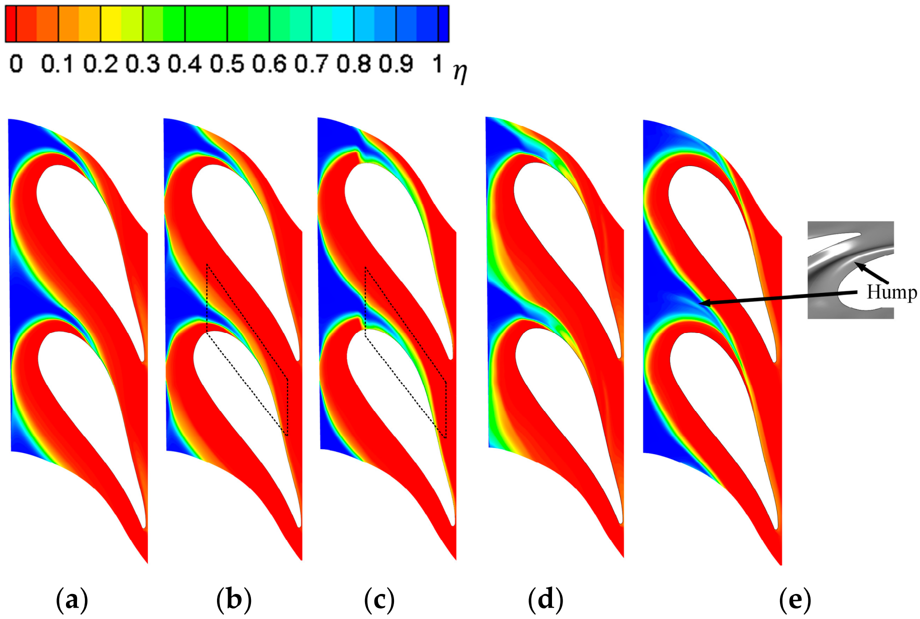


**Figure 10.** Film cooling effectiveness distributions on the endwall. (**a**) Initial contour. (**b**) Case 1. (**c**) Case 2. (**d**) Case 3. (**e**) Case 4.

Obviously, NECs will increase the surface area of endwalls. Hence, a dimensionless effective coolant coverage area $A_e$ is introduced to quantify the effects of the NEC on purge flow. An area of $\eta > 0.05$ is chosen as the effective coverage area of coolant, and the area from the outlet of the slot to the endwall of the trailing edge is $A_f$.

$$\overline{A_e} = A_e / A_f \tag{12}$$

Table 5 shows the increase in $\Delta\overline{A_e}$ by taking the effective coverage area of the flat endwall as the basis for different NECs. The results indicate that in Case 1, Case 2, and Case 4, the coverage area of the coolant can still be significantly increased by increasing the endwall surface area, and the maximum increase is observed in Case 4. Compared with Case 1, due to the weakening of the suction-side leg of the horseshoe vortex, Case 2's coverage area of coolant increased by 3.33%.

**Table 5.** The $\Delta\overline{A_e}$ of different non-axisymmetric endwalls.

| Case | $\Delta\overline{A_e}$/% |
|---|---|
| Case 1 | 8.41 |
| Case 2 | 11.74 |
| Case 3 | −4.13 |
| Case 4 | 28.29 |

To explain the influence of different NECs on the film cooling performance in more depth, the axial distribution of the laterally average film effectiveness of the flat endwall and the NECs are shown in Figure 11. Overall, Case 4 can improve the laterally averaged film effectiveness of the entire endwall compared to the flat endwall. Case 2 enhances the laterally averaged film effectiveness of region $Z/C_{ax} > 0.2$; for Case 1, although the area covered by coolant is increased, the global laterally averaged film effectiveness is decreased. Case 3 has the worst cooling performance, similar to what is observed in Figure 10. In addition, various NECs can improve the film cooling effectiveness in the range of $Z/C_{ax} > 0.75$.

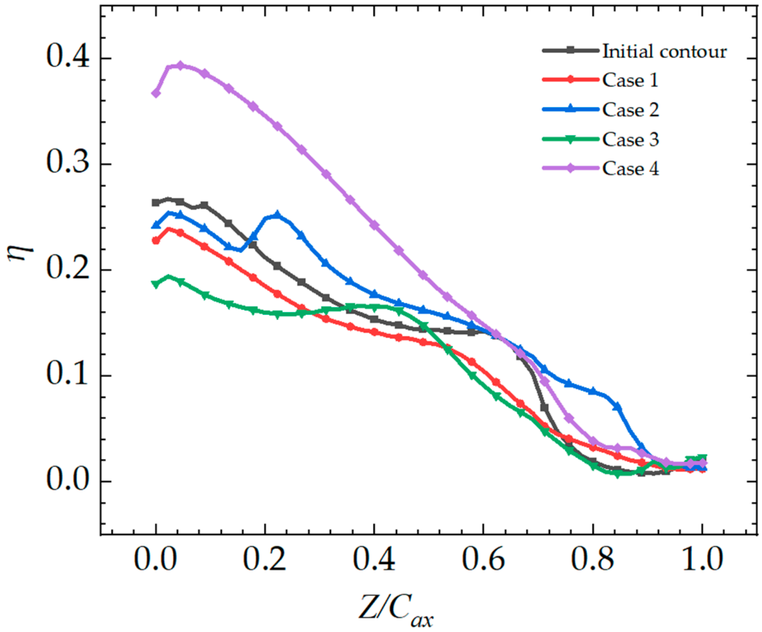


**Figure 11.** Axial distributions of laterally averaged film effectiveness on the endwalls.

### 3.3. *Effect of Slotting Angle on Gas Film Cooling Characteristics of Molded Endwall*

At a certain mass flow rate, the slotting angle will impact the mixing of purge flow and the mainstream flow, thus, affecting the endwall's cooling performance. Combining the conclusions in Section 3.2 with the aerodynamic and cooling characteristics, this section investigates the influence of 30°, 45°, and 60° angles (as shown in Figure 12) on the cooling characteristics in Case 1 and Case 2. In this section, the other parameters remain unchanged, with the exception of changing the incident angle of the slot, W = 10 mm.

Table 6 shows the increase based on the effective coverage area of the initial endwall at different incident angles—$\Delta\overline{A_e}$. Figure 13 states the purge flow cooling effectiveness distribution at different angles, and the results indicate that the angle has a great influence on the coverage of the coolant; under the 30° inclination angle, the momentum of the radial component of the coolant is the smallest. The coolant can better cover the endwall, and the film-cooling effectiveness on the pressure side is significantly increased. On the contrary, due to the large radial component's momentum at the 60° inclination angle, a small amount of coolant covers the endwall. In this context, Case 1 and Case 2 weaken the passage vortex, with a small amount of coolant on the endwall being fully diffused and protecting the downstream area of the suction surface.

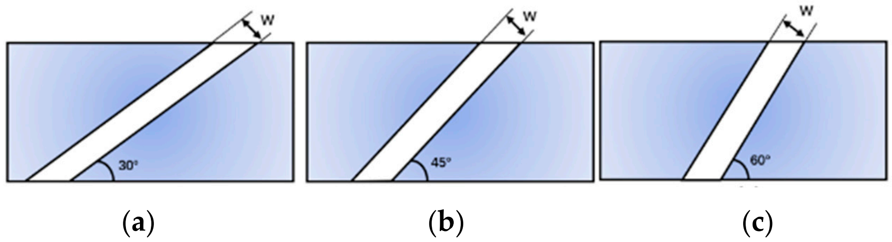


**Figure 12.** Schematic diagram of slotting angle. (**a**) Slotting angle = 30°. (**b**) Slotting angle = 45°. (**c**) Slotting angle = 60°.

**Table 6.** The $\Delta\overline{A_e}$ of different non-axisymmetric endwalls with variable Slotting angles.

| Case | $\Delta\overline{A_e}$/% |
|---|---|
| Initial contour-30° | 33.99 |
| Case 1-30° | 36.18 |
| Case 2-30° | 36.98 |
| Initial contour-60° | −27.22 |
| Case 1-60° | −22.55 |
| Case 2-60° | −19.71 |

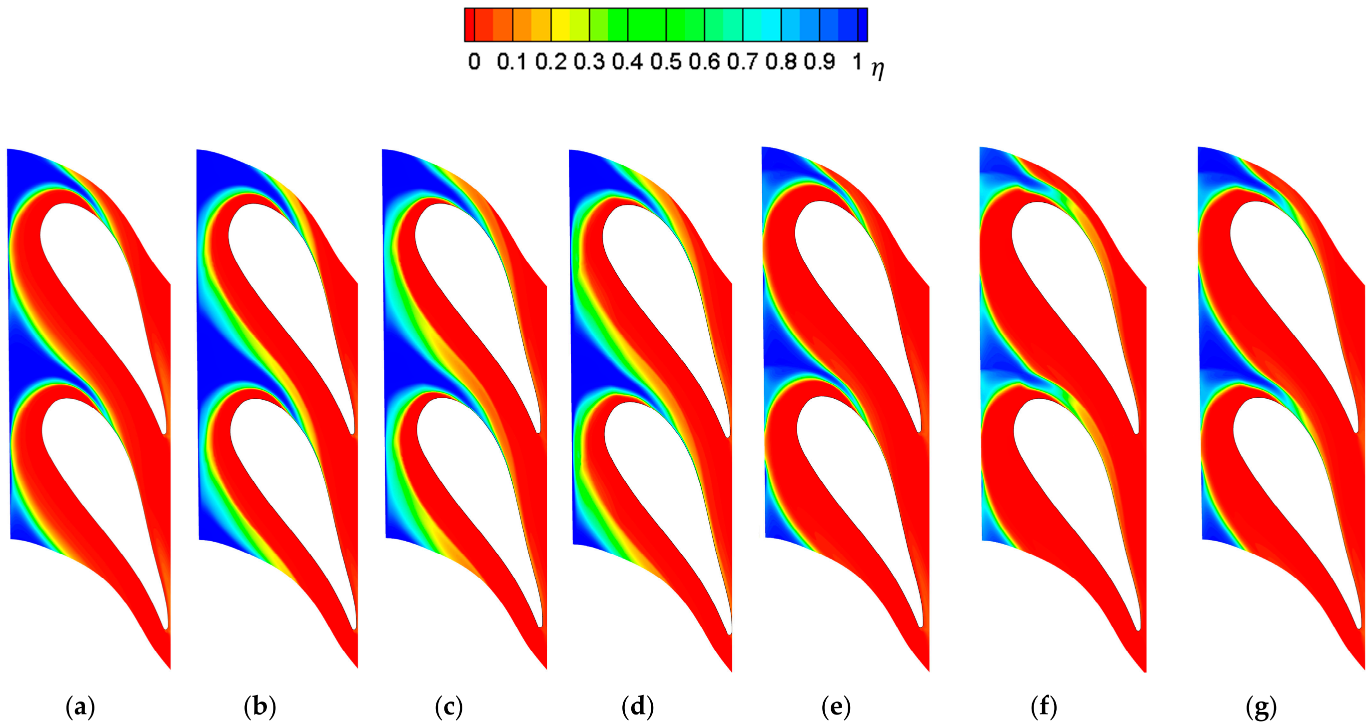


**Figure 13.** Film cooling effectiveness distributions on the endwall. (**a**) Initial contour. (**b**) Initial contour-30°. (**c**) Case 1-30°. (**d**) Case 2-30°. (**e**) Initial contour-60°. (**f**) Case 1-60°. (**g**) Case 2-60°.

To further illustrate the influence of different incident angles on the cooling performance in different areas of the endwall, Figure 14 shows the axial distribution of the laterally average film effectiveness of the endwall. The results show that the angle of 30° is favorable for coolant covering the endwall, and Cases 1 and 2 reduce the laterally averaged film effectiveness. When the inclination angle is 60°, Case 2 can improve the laterally averaged film effectiveness throughout the whole passage.

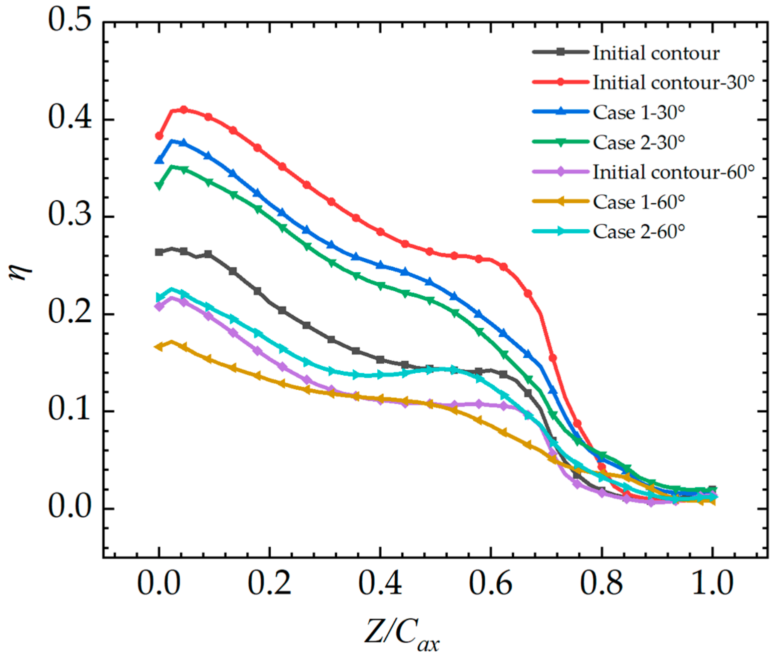


**Figure 14.** Axial distributions of laterally averaged film effectiveness on the endwall.

## 4. Conclusions

Based on the validated numerical method, the effectiveness of the proposed NECs is explored on a guide vane of a typical commercial engine. To better find the desirable solutions, different cases are compared from the aerodynamic and cooling characteristics. The main conclusions of this paper are drawn as follows:

(1) For the computational model of the study, the NEC based on differential pressure contouring can decrease the aerodynamic losses in the cascade by reducing the lateral pressure differences. Case 3 has the best aerodynamic characteristic, and the total pressure loss coefficient of the cascade is reduced by 0.305%.

(2) The NEC can significantly increase the coverage area for coolant, and Case 4 is up to 28.29% higher than the Initial contour. To balance the aerodynamic and cooling characteristics, Case 2 achieves the best outcome, with the total pressure loss coefficient of cascade being reduced by 0.272% and the non-dimensional effective coverage area of coolant increases by 11.74% compared to the baseline endwall.

(3) Endwall molding can improve the protective effect of a jet with a large slot angle but has no obvious effect on a jet with a small angle. Compared to the Initial contour-60°, the coverage area of coolant is increased by 7.51% with Case 2-60°. In contrast, based on the Initial contour-30°, Case 2-30° slightly enhances the coverage area of coolant by 2.99%.

Overall, this paper proposes an efficient non-axisymmetric endwall contouring approach through numerical simulation. In the near future, we will design relevant experiments to verify the effectiveness of the modeling method in this paper.

**Author Contributions:** Conceptualization, K.D. and Y.J.; methodology, Y.J.; software, H.S.; validation, L.C. and Q.Z.; formal analysis, T.C.; investigation, T.C.; resources, K.D.; data curation, Y.J.; writing—original draft preparation, Y.J.; writing—review and editing, K.D.; visualization, H.S.; supervision, C.L. All authors have read and agreed to the published version of the manuscript.

**Funding:** The authors gratefully acknowledge the support of the National Natural Science Foundation (No. 52006178) of China, the National Key R&D Program of China (No. Y2019-VIII-0007-0168), the Fundamental Research Funds for the Central Universities and the Innovation Capacity Support Plan in Shaanxi Province of China (Grant No. 2023-CX-TD-19).

**Institutional Review Board Statement:** Not applicable.

**Informed Consent Statement:** Not applicable.

**Data Availability Statement:** The data that support the findings of this study are available from the corresponding author upon reasonable request.

**Conflicts of Interest:** The authors declare no conflict of interest.

## References

1. Han, J.C. Advanced cooling in gas turbines 2016 max Jakob memorial award paper. *J. Heat Transfer.* **2018**, *140*, 113001. [CrossRef]
2. Wang, W.; Yan, Y.; Zhou, Y.; Cui, J. Review of Advanced Effusive Cooling for Gas Turbine Blades. *Energies* **2022**, *15*, 8568. [CrossRef]
3. Barigozzi, G.; Abdeh, H.; Rouina, S.; Franchina, N. The Aero-Thermal Performance of Purge Flow and Discrete Holes Film Cooling of Rotor Blade Platform in Modern High Pressure Gas Turbines: A Review. *Int. J. Turbomach. Propuls. Power* **2022**, *7*, 22. [CrossRef]
4. Chen, P.T.; Wang, L.; Li, X.Y.; Ren, J.; Jiang, H.D. Effect of axial turbine non-axisymmetric endwall contouring on film cooling at different locations. *Int. J. Heat Mass Transfer.* **2020**, *147*, 118995. [CrossRef]
5. Denton, J.D. Loss Mechanisms in Turbomachines. In Proceedings of the ASME 1993 International Gas Turbine and Aeroengine Congress and Exposition, Cincinnati, OH, USA, 24–27 May 1993.
6. Rose, M.G. Non-axisymmetric end wall profiling in the HP NGVs of an axial flow gas turbine. In Proceedings of the ASME 1994 International Gas Turbine and Aeroengine Congress and Exposition, The Hague, Netherlands, 13–16 June 1994.
7. Harvey, N.W.; Rose, M.G.; Taylor, M.D.; Shahpar, S.; Hartland, J.; Gregory-Smith, D.G. Non-axisymmetric Turbine End Wall Design: Part I-Three Dimensional Linear Design System. In Proceedings of the ASME 1999 International Gas Turbine and Aeroengine Congress and Exhibition, Indianapolis, IN, USA, 7–10 June 1999.
8. Chen, P.T.; Zhao, K.; Li, X.Y.; Ren, J.; Jiang, H.D. Effects of varying non-axisymmetric contours of the turbine endwall on aerodynamics and heat transfer Aspects: A sensitivity analysis study. *Int. J. Therm. Sci.* **2021**, *161*, 106689. [CrossRef]
9. Ahn, J. Large Eddy Simulation of Film Cooling: A Review. *Energies* **2022**, *15*, 8876. [CrossRef]
10. Zhang, C.; Wang, W.; Wang, Z.; Tong, Z. Conjugate Heat Transfer Simulation of Overall Cooling Performance for Cratered Film Cooling Holes. *Machines* **2022**, *10*, 395. [CrossRef]
11. Zhao, L.; Ma, H. Experimental Investigation of the Effect of Purge Flow and Main Flow Interaction in a Low-Speed Turbine Cascade Passage. *Entropy* **2020**, *22*, 623. [CrossRef] [PubMed]
12. Sundaram, N.; Thole, K.A. Bump and Trench Modifications to Film Cooling Holes at the Vane-Endwall Junction. In Proceedings of the ASME Turbo Expo 2007: Power for Land, Sea, and Air, Montreal, Canada, 14–17 May 2007.
13. Du, K.; Song, L.M.; Li, J.; Sunden, B. Effects of the mainstream turbulence intensity and slot injection angle on the endwall cooling and phantom cooling of the vane suction side surface. *Int. J. Heat Mass Transfer.* **2017**, *112*, 427–440. [CrossRef]
14. Tao, Z.; Yao, Y.J.; Zhu, P.Y.; Song, L.M.; Li, J. Experimental and numerical study on film cooling effectiveness of an annular cascade endwall with different slot configuration. *Int. J. Therm. Sci.* **2020**, *158*, 106517. [CrossRef]
15. Babu, S.; Kiran, K.N.; Tom, J.K.; Anish, S. Numerical Investigation on Effects of Profiled Endwall Over Purge Flow in Linear Turbine Cascade. In Proceedings of the 7th Asian Joint Workshop on Thermophysics and Fluid Science, Trivandrum, India, 24 November 2018.
16. Zhang, K.Y.; Li, Z.G.; Li, J. Non-axisymmetric endwall contour optimization and performance assessment as affected by simulated swirl purge flow and backward hole injection. *Int. J. Therm. Sci.* **2022**, *172*, 107297. [CrossRef]
17. Tao, Z.; Guo, Z.D.; Yu, B.Y.; Song, L.M.; Li, J. Aero-Thermal Optimization of a Gas Turbine Blade Endwall with Non-Axisymmetric Contouring and Purge Flow. *Int. J. Heat Mass Transfer.* **2021**, *178*, 121626. [CrossRef]
18. Mensch, A.; Thole, K.A. Overall Effectiveness and Flowfield Measurements for an Endwall with Non-axisymmetric Contouring. In Proceedings of the ASME Turbo Expo 2015: Turbine Technical Conference and Exposition, Montreal, QC, Canada, 15–19 June 2015.
19. Du, K.; Li, J. Numerical study on the effects of slot injection configuration and endwall alignment mode on the film cooling performance of vane endwall. *Int. J. Heat Mass Transfer.* **2016**, *98*, 768–777. [CrossRef]